

White-light Sagnac interferometer for snapshot polarimetric and multispectral imaging

Michael W. Kudenov¹, Matthew E. L. Jungwirth¹, Eustace L. Dereniak¹, Grant R. Gerhart²

¹The University of Arizona, College of Optical Sciences, 1630 E. University Blvd., Tucson, AZ

²U.S. Army TARDEC/RDECOM, AMSRD-TAR/MS 263, Warren, MI 48397-5000

ABSTRACT

A common technique, referred to as channeled imaging polarimetry (CIP), enables the snapshot acquisition of the 2-dimensional Stokes parameters of an arbitrary scene or sample. It achieves this by amplitude modulating the Stokes parameters onto various interference-based spatial carrier frequencies. While this technique has utility, it often suffers from low signal-to-noise ratios, in remote sensing scenarios, due to its requirement of narrow spectral bandwidth illumination (< 3 nm in the visible). This paper discusses one hardware implementation that can be utilized to overcome this limitation. Consequently, an overview of the theoretical and experimental development of a unique Sagnac interferometer is discussed. Both laboratory and outdoor data are included to demonstrate the instrument's ability to measure polarization in arbitrary scenes. Inclusion of blazed diffraction gratings inside the interferometer enables white-light interference fringes to be generated. By incorporating these gratings, the operational bandwidth of the interference fringes can exceed approximately 300 nm; two orders of magnitude greater than previous CIP implementations. Lastly, by modifying the diffraction grating, the sensor becomes capable of snapshot multispectral imaging. This will be briefly discussed, with both a theoretical description and experimental data.

Keywords: Stokes, polarimetry, interferometry, Sagnac interferometer, Savart plate.

1.0 INTRODUCTION

Instantaneous acquisition of the Stokes polarization parameters is of great interest in many areas of remote sensing [1]. A Stokes imaging polarimeter is capable of obtaining either the partial or complete polarization state of a scene via four Stokes parameters. These parameters express the state of polarization in a 4x1 matrix, defined as

$$\mathbf{S}(x, y) = \begin{bmatrix} S_0(x, y) \\ S_1(x, y) \\ S_2(x, y) \\ S_3(x, y) \end{bmatrix} = \begin{bmatrix} I_0(x, y) + I_{90}(x, y) \\ I_0(x, y) - I_{90}(x, y) \\ I_{45}(x, y) - I_{135}(x, y) \\ I_R(x, y) - I_L(x, y) \end{bmatrix} \quad (1)$$

where x, y are spatial coordinates in the scene, S_0 is the total energy of the beam, S_1 denotes preference for linear 0° over 90°, S_2 for linear 45° over 135°, and S_3 for circular right over left polarization states. Each is defined by an addition or subtraction of intensity measurements that represent different analyzer states, and complete characterization requires at least four such states be measured. These measurements can be acquired over time by use of a rotating element (division of time) with a single imaging lens and focal plane array (FPA). Such an implementation yields a compact and relatively inexpensive instrument. However, these sensors are susceptible to misregistration errors caused by platform or scene motion, since in many applications, Stokes parameters are acquired from moving platforms.

One method of acquiring all the Stokes parameters simultaneously, discovered by K. Oka, is by amplitude modulating the Stokes parameters onto carrier frequencies [2]. Oka established that the complete Stokes vector can be encoded onto various interference fringes with the use of two Savart plates located within a collimated space of an optical system [3]. This provides the advantage of being snapshot, while also offering inherent image registration since the Stokes parameters are encoded on coincident fringe fields. However, one previously unresolved concern is that the carrier frequency's visibility decreases as the coherence length of the incident illumination is decreased. Therefore, high-visibility fringes are generated only when the light is quasi-monochromatic, leading to a reduced signal-to-noise ratio in remote sensing applications. This is especially a concern for operation of the sensor in the thermal infrared (3-12 μ m) [4].

Report Documentation Page		<i>Form Approved OMB No. 0704-0188</i>
<p>Public reporting burden for the collection of information is estimated to average 1 hour per response, including the time for reviewing instructions, searching existing data sources, gathering and maintaining the data needed, and completing and reviewing the collection of information. Send comments regarding this burden estimate or any other aspect of this collection of information, including suggestions for reducing this burden, to Washington Headquarters Services, Directorate for Information Operations and Reports, 1215 Jefferson Davis Highway, Suite 1204, Arlington VA 22202-4302. Respondents should be aware that notwithstanding any other provision of law, no person shall be subject to a penalty for failing to comply with a collection of information if it does not display a currently valid OMB control number.</p>		
1. REPORT DATE 15 MAR 2010	2. REPORT TYPE Journal Article	3. DATES COVERED 15-03-2010 to 15-03-2010
4. TITLE AND SUBTITLE WHITE-LIGHT SAGNAC INTERFEROMETER FOR SNAPSHOT POLARIMETRIC AND MULTISPECTRAL IMAGING		5a. CONTRACT NUMBER
		5b. GRANT NUMBER
		5c. PROGRAM ELEMENT NUMBER
6. AUTHOR(S) Michael Kudenov; Matthew Jungwirth; Eustace Dereniak; Grant Gerhart		5d. PROJECT NUMBER
		5e. TASK NUMBER
		5f. WORK UNIT NUMBER
7. PERFORMING ORGANIZATION NAME(S) AND ADDRESS(ES) University Of Arizona,College of Optical Sciences,1630 E. University Blvd. ,Tucson,AZ,85721		8. PERFORMING ORGANIZATION REPORT NUMBER ; #20607
9. SPONSORING/MONITORING AGENCY NAME(S) AND ADDRESS(ES) U.S. Army TARDEC, 6501 E.11 Mile Rd, Warren, MI, 48397-5000		10. SPONSOR/MONITOR'S ACRONYM(S) TARDEC
		11. SPONSOR/MONITOR'S REPORT NUMBER(S) #20607
12. DISTRIBUTION/AVAILABILITY STATEMENT Approved for public release; distribution unlimited		
13. SUPPLEMENTARY NOTES Submitted to SPIE Aerospace Conference		
14. ABSTRACT A common technique, referred to as channelled imaging polarimetry (elP), enables the snapshot acquisition of the 2- dimensional Stokes parameters of an arbitrary scene or sample. It achieves this by amplitude modulating the Stokes parameters onto various interference-based spatial carrier frequencies. While this technique has utility, it often suffers from low signal-to-noise ratios, in remote sensing scenarios, due to its requirement of narrow spectral bandwidth illumination (< 3 nm in the visible). This paper discusses one hardware implementation that can be utilized to overcome this limitation. Consequently, an overview of the theoretical and experimental development of a unique Sagnac interferometer is discussed. Both laboratory and outdoor data are included to demonstrate the instrument's ability to measure polarization in arbitrary scenes. Inclusion of blazed diffraction gratings inside the interferometer enables whitelight interference fringes to be generated. By incorporating these gratings, the operational bandwidth of the interference fringes can exceed approximately 300 nm; two orders of magnitude greater than previous CIP implementations. Lastly by modifying the diffraction grating, the sensor becomes capable of snapshot multispectral imaging. This will be briefly discussed, with both a theoretical description and experimental data.		
15. SUBJECT TERMS Stokes. polarimetry, interferometry, Sagnac interferometer, Savart plate.		

16. SECURITY CLASSIFICATION OF:			17. LIMITATION OF ABSTRACT Same as Report (SAR)	18. NUMBER OF PAGES 9	19a. NAME OF RESPONSIBLE PERSON
a. REPORT unclassified	b. ABSTRACT unclassified	c. THIS PAGE unclassified			

Standard Form 298 (Rev. 8-98)
Prescribed by ANSI Std Z39-18

In this paper, we discuss the theoretical and experimental development of a dispersion compensated Sagnac interferometer. In section 2, we discuss the use of a Sagnac interferometer as a replacement for a Savart plate in K. Oka's original implementation. In section 3, the dispersion compensated Sagnac polarization interferometer (DCPSI) is introduced, and its theoretical background is provided. In section 4, an interesting aspect of the DCPSI is investigated, in that it can be applied for use as a multispectral imager. Lastly, section 5 highlights experimental results from both systems.

2.0 SAGNAC INTERFEROMETER AS A SAVART PLATE

A Sagnac interferometer with polarization optics can duplicate the shearing and optical properties of a Savart plate (SP) [5, 6, 7]. Such a polarization Sagnac interferometer (PSI) is portrayed in Fig. 1.

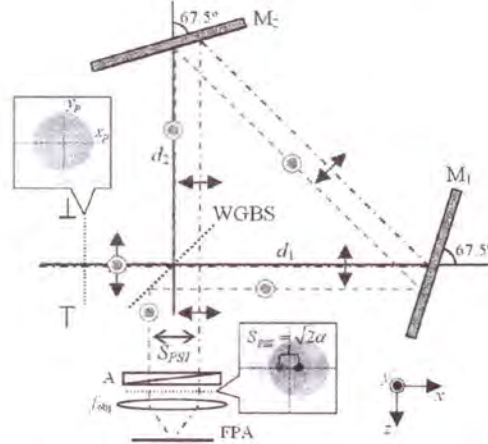


Fig. 1. A polarization Sagnac interferometer. The distance between the WGBS and mirrors, M_1 and M_2 , is denoted d_1 and d_2 , respectively. A shear (S_{PSI}) is produced when $d_1 \neq d_2$. The case $d_1 > d_2$ is illustrated, with $d_1 = d_2 + \alpha$. [8]

The PSI contains two mirrors, M_1 and M_2 , at the output faces of a wire grid beam splitter (WGBS). It also contains a lens with a focal length, f_{obj} , which is used to image the source or scene onto a focal plane array (FPA). The two beams are separated by a shear, S_{PSI} , when $d_1 \neq d_2$. If $d_1 = d_2 + \alpha$, where α is some distance that mirror M_1 was translated, then the shear is

$$S_{PSI} = \sqrt{2}\alpha \quad (2)$$

Note that this shear is independent of the wavelength of the incident illumination [9]. The optical path difference (OPD) between the two sheared beams emerging from the PSI is given by

$$OPD = S_{PSI} \sin(\theta) \approx S_{PSI} \theta. \quad (3)$$

When the two sheared beams are imaged onto the FPA by the lens, they combine and produce interference at the image plane. The intensity at the FPA is described by

$$I_{PSI}(x_i, y_i) = \frac{1}{2} \left[S_0 + S_2 \cos\left(\frac{2\pi}{\lambda f_{obj}} \sqrt{2}\alpha x_i\right) - S_3 \sin\left(\frac{2\pi}{\lambda f_{obj}} \sqrt{2}\alpha x_i\right) \right]. \quad (4)$$

where S_0 , S_1 , and S_3 are implicitly dependent upon spatial coordinates x_i and y_i . Fourier transformation of this interference pattern produces multiple carrier frequencies in the spatial frequency domain. Filtration of these peaks, followed by an inverse Fourier transform, enables the incident Stokes parameters to be extracted. [3] A carrier frequency, U_{PSI} , can be described as

$$U_{PSI} = \frac{\sqrt{2}\alpha}{\lambda f_{obj}}, \quad (5)$$

Notable is the inverse relationship to the wavelength. This dispersion in the spatial carrier frequency causes a visibility reduction in the fringes that are modulating the incident Stokes parameters. When the carrier frequency visibility is reduced to zero, the incident Stokes parameter becomes irrecoverable. This typically occurs for spectral bandwidths exceeding approximately 3 nm. To remedy concerns related to the narrow spectral bandwidth, the shear must be made linearly proportional to the wavelength, such that $S_{PSI} \propto \lambda \gamma$, where γ is some optical thickness, analogous to α .

3.0 DISPERSION COMPENSATION IN THE SAGNAC INTERFEROMETER

Removing the dispersion in the PSI's carrier frequency can be achieved by introducing two blazed diffraction gratings into each arm of the interferometer. Diffraction gratings have been used in past experiments to generate white-light interference fringes, specifically for optical testing [10]. The new interferometer, referred to as the dispersion-compensated polarization Sagnac interferometer (DCPSI), is depicted in Fig. 2. In this case, the WGBS to mirror M_1 and M_2 separations (d_1 and d_2 in Fig. 1) are set equal, and the shear is generated exclusively by the diffraction gratings, G_1 and G_2 . A ray's diffraction angle, after transmission through either grating, is calculated by

$$\sin(\theta) = \frac{m\lambda}{d}, \quad (6)$$

where θ is the diffraction angle of the ray as measured from the grating's normal, m is the order of diffraction, and d is the period of the grating. Since d is typically large ($\approx 30 \mu\text{m}$), small angle approximations can be used to simplify Eq. 6, yielding $\theta \approx m\lambda/d$.

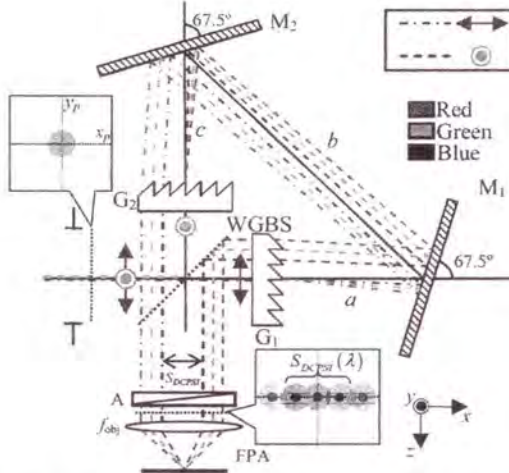


Fig. 2. DCPSI with blazed diffraction gratings, G_1 and G_2 , positioned at each output of the WGBS. Inclusion of the gratings generates a shear that is directly proportional to the wavelength.

In the DCPSI, the spectrally broadband beam reflected by the WGBS is initially diffracted by grating G_2 into the +1 order. These dispersed rays propagate through the system to grating G_1 , where they are diffracted into the 0-order, thus removing the diffraction angle imposed by G_2 . The rays exit the system parallel to the optical axis, but offset by a distance proportional to λx_o , where x_o is some constant related to the DCPSI's configuration. Conversely, the beam transmitted by the WGBS is initially incident and diffracted by G_1 , and exits the system offset by $-\lambda x_o$. The functional form of the shear, calculated by unfolding the optical system, is expressed as

$$S_{DCPSI} = 2 \frac{m\lambda}{d} (a + b + c) \quad (7)$$

where a , b , and c represent the distances between G_1 and M_1 , M_1 and M_2 , and M_2 and G_2 , respectively. Consequently, the DCPSI can generate a shear that is linearly dependent upon wavelength to first-order. The intensity on the FPA can then be expressed as

$$I_{DCPSI}(x_i, y_i) = \frac{1}{2} \sum_{m=0}^{d/\lambda_1} S'_0(m) + \frac{1}{2} \sum_{m=1}^{d/\lambda_2} \left[S'_2(m) \cos \left(\frac{2\pi}{f_{obj}} \frac{2m}{d} (a+b+c) x_i \right) - S'_3(m) \sin \left(\frac{2\pi}{f_{obj}} \frac{2m}{d} (a+b+c) x_i \right) \right] \quad (8)$$

where the total intensity pattern is a summation from the minimum to maximum order of a blazed grating, such that the maximum achievable order is $(d/\lambda_1)\sin(\pi/2)$, where λ_1 is the minimum wavelength passed by the optical system and $S_0(m)$, $S_2(m)$, and $S_3(m)$ are the Stokes parameters weighted by the diffraction efficiency (DE) of both gratings before integration over wavelength,

$$S'_0(m) = \int_{\lambda_1}^{\lambda_2} DE^2(\lambda, m) S_0(\lambda) d\lambda \quad (9)$$

$$S'_2(m) = \int_{\lambda_1}^{\lambda_2} DE^2(\lambda, m) S_2(\lambda) d\lambda \quad (10)$$

$$S'_3(m) = \int_{\lambda_1}^{\lambda_2} DE^2(\lambda, m) S_3(\lambda) d\lambda \quad (11)$$

where λ_1 and λ_2 denote the minimum and maximum wavelengths passed by the optical system. The carrier frequency, U_{DCPSI} , is

$$U_{DCPSI} = \frac{2m}{df_{obj}} (a+b+c). \quad (12)$$

Therefore, inserting the blazed diffraction gratings into the optical system enables cancellation of the dispersion term in the denominator. Another interesting aspect of the carrier frequency is that it depends upon the order of diffraction, m , which can be exploited for multispectral imaging.

4.0 MULTISPECTRAL DCPSI

In the polarimetric DCPSI, it is advantageous to utilize a single-order blazed grating optimized for the +1 diffraction order, which should be blazed for a wavelength in the middle of the spectral operating regime. However, if a multiple-order diffraction grating is used (*i.e.* a grating with a larger phase depth), then larger diffraction orders (*e.g.*, $m = 4, 5, 6$ etc.) would be observed in the system. Each one of these orders corresponds to a different blaze wavelength, such that $\lambda_m = \lambda_1/m$. Since each order that is observed on the image plane contains a different spatial carrier frequency, then each diffraction order can be treated as a unique spectral passband.

An illustration of the ideal diffraction efficiencies for the gratings used in the experiments is depicted in Fig. 3. Fig. 3 (a) portrays the diffraction efficiencies of the single-order blazed grating used in the DCPSI, while Fig. 3 (b) provides the diffraction efficiencies for the multiple-order blazed grating used in the MSI.

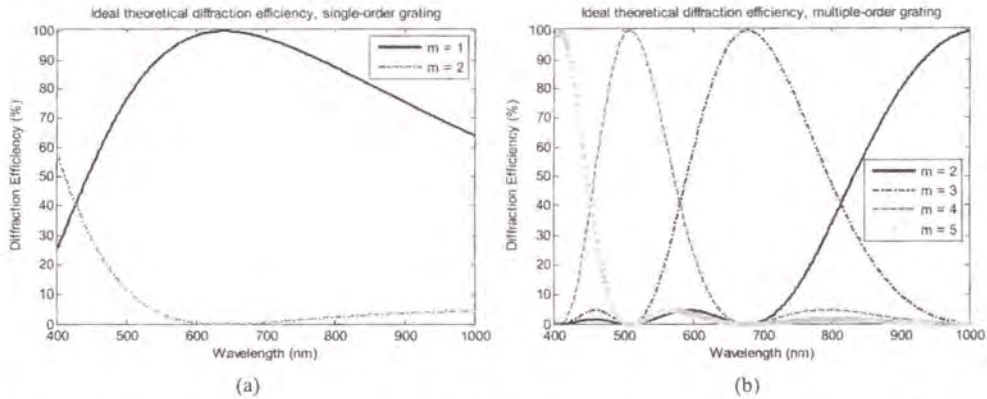


Fig. 3. (a) Diffraction efficiency (percent) for the blazed gratings used in the experimental results of the (a) single-order DCPSI and (b) multiple-order MSI. [11]

The configuration for the MSI is depicted in Fig. 4, and is similar to the DCPSI per Fig. 2 except for the inclusion of the multiple-order gratings. Additionally, a linear polarizer (LP) at 45° is also included to uniformly polarize the incident illumination. This makes the intensity pattern on the FPA equal to,

$$I_{MSI}(x_i, y_i) = \frac{1}{2} \sum_{m=0}^{\text{Ceil}[\lambda_i/\lambda_{\min}]} [S_0^*(m)] + \frac{1}{2} \sum_{m=1}^{\text{Ceil}[\lambda_i/\lambda_{\min}]} \left[S_0^*(m) \cos \left(\frac{2\pi}{f_{\text{obj}}} \frac{2m}{d} (a+b+c) x_i \right) \right], \quad (13)$$

where

$$S_0^*(m) = \int_{\lambda_1}^{\lambda_2} DE^2(\lambda, m)(S_0(\lambda) + S_2(\lambda))d\lambda \quad (14)$$

and the *dominant* orders experimentally observed in the system correspond to the ceiling (Ce) of λ_1/λ_{\min} , where λ_1 is the first order blaze wavelength of the diffraction grating. This changes the maximum limit of the summation from d/λ_{\min} to $Ce[\lambda_1/\lambda_{\min}]$ observed in Eq. 13. For small incident S_2 , the measurement corresponds to S_0 , or the unpolarized component of the incident illumination. It should be noted that a polarization insensitive design can be produced by replacing the WGBS with a standard 50/50 beamsplitter.

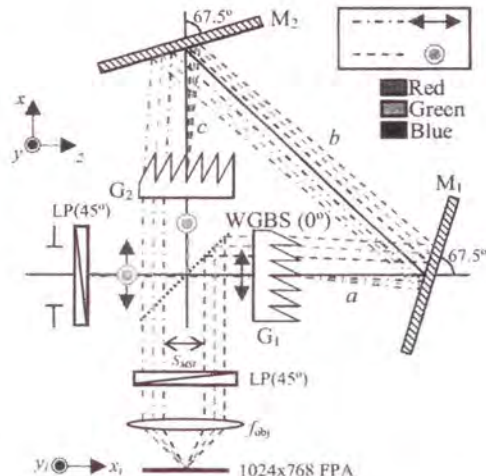


Fig. 4. MSI configuration. The single-order gratings of the DCPSI are replaced with multiple-order (higher phase-depth) gratings. [11]

5.0 EXPERIMENTAL RESULTS

To verify the operating principles of the DCPSI and MSI, an experimental setup was configured for each variant of the system. For the DCPSI, the polarimetric accuracy was assessed, while with the MSI, the spectral reflectance accuracy was studied.

5.1 DCPSI

The experimental configuration for the DCPSI is depicted in Fig. 5. From Fig. 5, spatially and temporally incoherent light is setup through the use of a reflective diffuser. A dichroic polymer linear polarizer, oriented at 45° , followed by an achromatic quarter-wave retarder (QWR) at θ_G , is used to generate input polarization states for testing and validation. The WGBS has a clear aperture of approximately 21 mm and is anti-reflection coated for 400-700 nm. Mirrors M_1 and M_2 consist of $1/10^{\text{th}}$ wave optical flats, while a collimating lens ($f_c = 50 \text{ mm}$) is used to image the object plane to infinity. An objective lens ($f_{\text{obj}} = 200 \text{ mm}$) is used for re-imaging onto the FPA, thus yielding a field of view (FOV) of approximately $\pm 1^\circ$. The IR blocking filter rejects wavelengths beyond 750 nm from entering the objective lens.

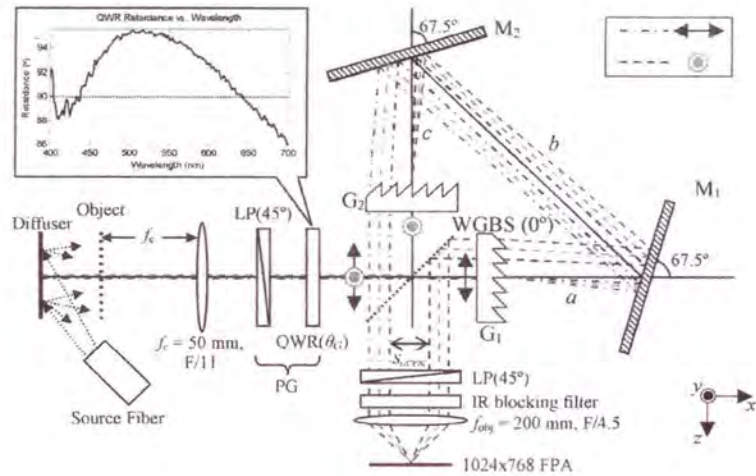


Fig. 5. Experimental setup for laboratory testing of the DCPSI using white light. The distances a , b , and c are 14.4 mm, 57.2 mm, and 12.9 mm, respectively.

First, an experimental verification of the white-light nature of the carrier frequency was preformed. This consisted of placing a monochromator in front of the instrument. Scanning the monochromator from 460-700 nm in 10 nm increments, while measuring the frequency of the interference fringe, yielded the results depicted in Fig. 6 for the DCPSI's carrier frequency (U_{DCPSI}). For comparison, the calculated carrier frequency, as a function of wavelength, for a standard PSI (U_{PSI}) is also included. Using the theoretical data, the carrier frequency's total peak-to-peak variation for the uncompensated PSI was calculated to be $11.31\text{E}3 \text{ m}^{-1}$. Conversely, the total variation in the carrier frequency of the DCPSI was measured to be 23.61 m^{-1} . Consequently, the total variation in the carrier frequency for the DCPSI is over two orders of magnitude lower than in the uncompensated PSI.

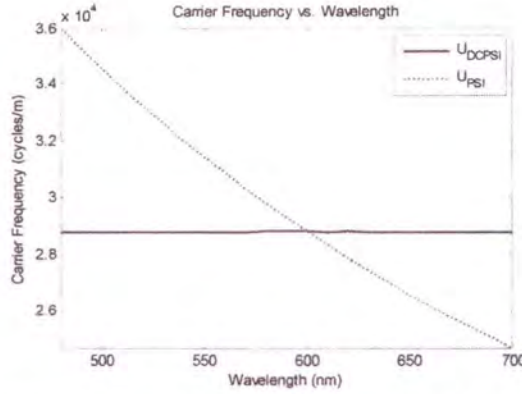


Fig. 6. Measured carrier frequency vs. wavelength for the DCPSI (solid dark-gray line) and the theoretical carrier frequency for a PSI (dotted light-gray line). The PSI's carrier frequency was set to equal the DCPSI's carrier frequency at a wavelength of 600 nm.

Data of outdoor targets were also obtained with the instrument. Data taken of a moving vehicle is depicted in Fig. 7. Here, the achromatic quarter-wave retarder (QWR) was used at the entrance of the system, positioned in front of the WGBS, enabling S_3 in Eq. 8 to be converted into S_2 . Thus, a complete linear polarimeter that can simultaneously measure S_0 , S_1 , and S_2 is produced [12].

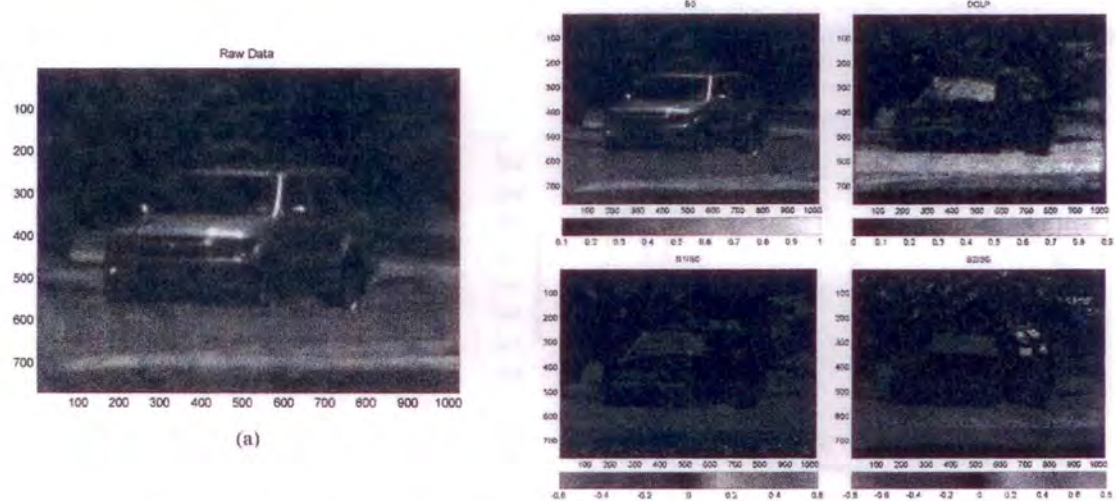


Fig. 7. (a) Raw data of a vehicle outdoors. (right panel) Processed polarization data of the vehicle, calculated from the data in (a). From the image in the first row and first column and moving clockwise: S_0 , DOLP, S_2/S_0 , and S_1/S_0 .

5.2 MSI

The experimental configuration for the MSI is depicted in Fig. 8. Here, spatially and temporally incoherent illumination is used to illuminate a target that is to be measured in reflectance. Furthermore, the objective lens' focal length is increased to $f_{\text{obj}} = 250$ mm, such that the higher diffraction orders appear as a lower frequency. Otherwise, all other specifications for the WGBS and mirrors are identical to the DCPSI's experimental configuration.

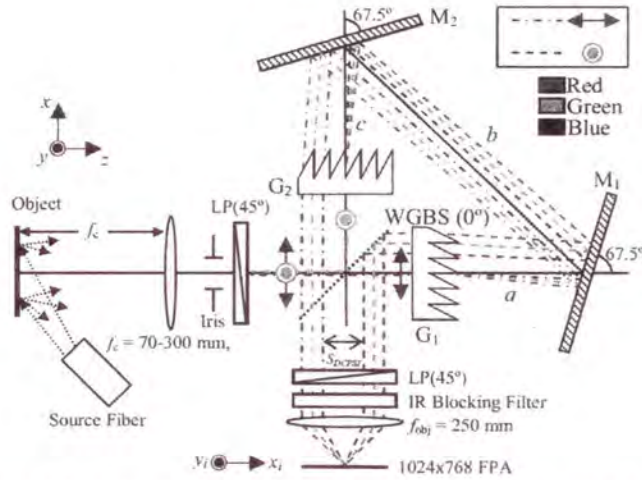


Fig. 8. Experimental setup of the MSI with a , b , and c set to 13.3 mm, 51.4 mm, and 19.1 mm, respectively. An IR blocking filter keeps wavelengths > 750 nm from entering the system [11]

In order to measure the relative spectral responsivity of the MSI's spectral passbands, the exit slit of a radiometrically calibrated monochromometer was placed within the object plane. The output of the monochromometer is depicted in Fig. 9 (a). This enabled the carrier frequencies to be observed and measured, where the absolute value of their amplitude in the Fourier domain was utilized to determine their spectral response. These responsivity measurements are depicted in Fig. 9 (b). As predicted from the ideal diffraction efficiencies depicted previous in Fig. 3 (b), four bands are present within the system.

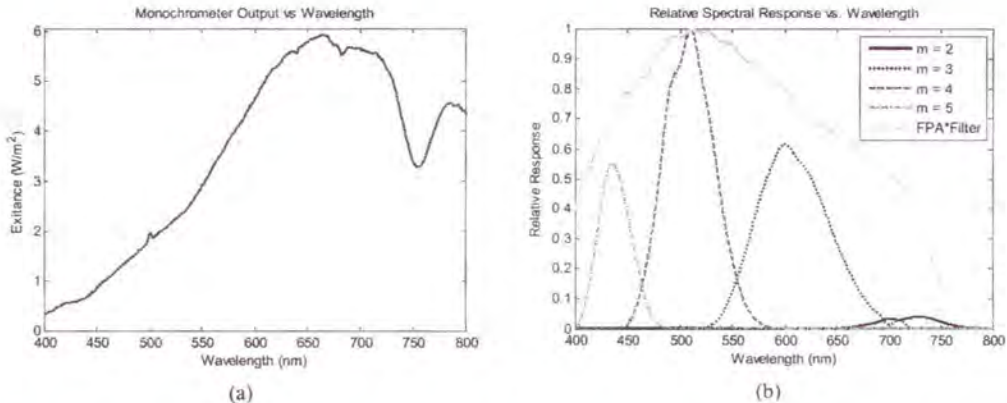


Fig. 9. (a) Measured monochrometer output in W/m^2 . (b) Measured relative spectral response of the different passbands within the MSI. Also included (solid light-gray line) is the relative response of the FPA multiplied by the measured transmission of the IR blocking filter. [11]

In order to investigate the accuracy of the multispectral data, a reflectance measurement from a healthy and unhealthy leaf was taken with the MSI, and compared to a calibrated non-imaging spectrometer. The measured passbands, previously indicated in Fig. 9 (b), were used to weight the data from the spectrometer. This relative reflectance measurement is depicted in Fig. 10.

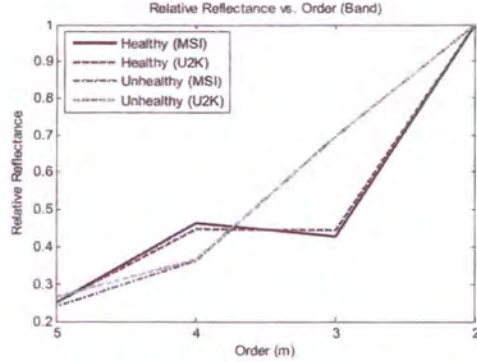


Fig. 10. Relative reflectance of the healthy and unhealthy leaves, normalized to the irradiance in order 2, as measured with the MSI and U2S. The healthy vegetation experiences more absorption in order 3 due to the presence of chlorophyll. [11]

The root mean square (RMS) error between the MSI and calibrated spectrometer data is calculated by

$$\varepsilon = \sqrt{\frac{1}{4} \sum_{m=2}^5 (R_{U2S}(m) - R_{MSI}(m))^2}. \quad (15)$$

The RMS error for the healthy and unhealthy leaf samples yields 0.0115 and 0.0117, respectively. Consequently, the error in the spectral reconstruction is on the order of 1.2 percent between the U2S and the MSI. A 2D photo of the healthy and unhealthy leaf was also taken, and can be observed in Fig. 11. The healthy leaf has a lower reflectance in the $m = 3$ (red) band due to the presence of chlorophyll.

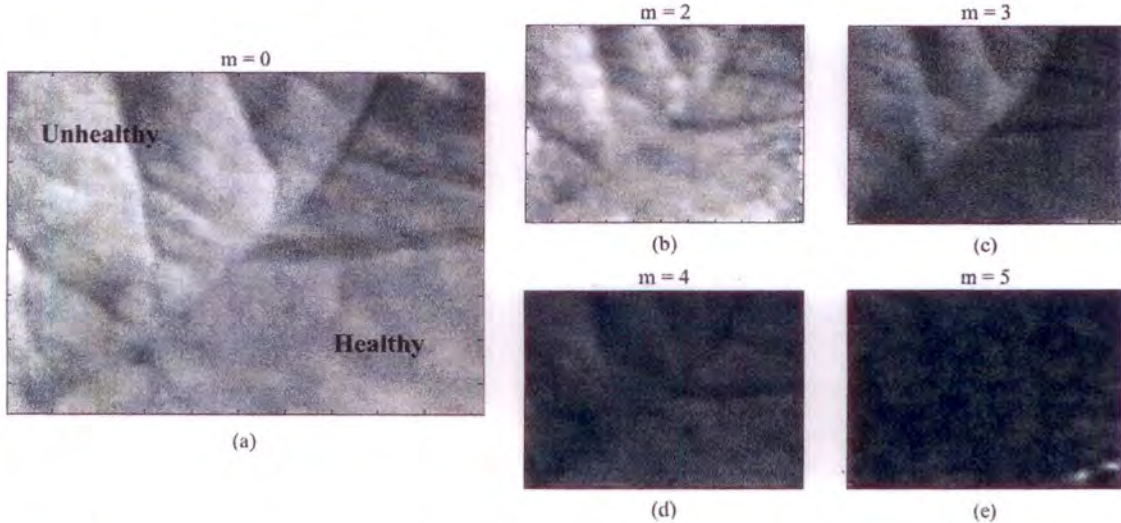


Fig. 11. Relative reflectance images of a healthy and unhealthy leaf. (a) Band-integrated image ($m = 0$). (b) - (e) Image from each order, $m = 2$ through $m = 5$, respectively. [11]

6.0 CONCLUSION

The development of a snapshot imaging linear polarimeter, based on channeled imaging polarimetry (CIP), has been overviewed. By incorporating blazed diffraction gratings into each arm of a Sagnac interferometer, it has demonstrated that white-light, broadband operation of the CIP technique can be implemented. Furthermore, by implementing multiple-order diffraction gratings into the system, a snapshot multispectral imager can be realized. Similar to how CIP modulates Stokes parameters onto spatial carrier frequencies, the multispectral implementation of the sensor produces a unique spatial carrier frequency for each spectral band.

REFERENCES

1. J. S. Tyo, D. L. Goldstein, D. B. Chenault, and J. A. Shaw, "Review of passive imaging polarimetry for remote sensing applications," *Appl. Opt.* **45** (22), 5453-5469 (2006).
2. K. Oka and T. Kato, "Spectroscopic polarimetry with a channeled spectrum," *Opt. Lett.* **24** (21), 1475-1477 (1999).
3. K. Oka and N. Saito, "Snapshot complete imaging polarimeter using Savart plates," *Proc. SPIE* **6295**, 629508 (2006).
4. M. W. Kudenov, L. Pezzaniti, E. L. Dereniak, and G. R. Gerhart, "Prismatic imaging polarimeter calibration for the infrared spectral region," *Opt. Exp.* **16**, 13720-13737 (2008).
5. G. Zhan, K. Oka, T. Ishigaki, and N. Baba, "Static Fourier-transform spectrometer based on Savart polariscope," *Proc. SPIE* **4480**, 198-203 (2002).
6. R. Suda, N. Saito, and K. Oka, "Imaging Polarimetry by Use of Double Sagnac Interferometers," in Extended Abstracts of the 69th Autumn Meeting of the Japan Society of Applied Physics (Japan Society of Applied Physics, Tokyo), p. 877 (2008).
7. M. Mujat, E. Baleine, and A. Dogariu, "Interferometric imaging polarimeter," *J. Opt. Soc. Am. A* **21** (11), 2244-2249 (2004).
8. M. W. Kudenov, M. E. L. Jungwirth, E. L. Dereniak, and G. R. Gerhart, "White light Sagnac interferometer for snapshot linear polarimetric imaging," *Opt. Exp.* **17** (25) pp. 22520-22534 (2009).
9. M. Born and E. Wolf, *Principles of Optics* (Cambridge University Press, 1999), p. 831.
10. J. C. Wyant, "OTF measurements with a white light source: an interferometric technique," *Appl. Opt.* **14** (7), 1613-1615 (1975).
11. M. W. Kudenov, College of Optical Sciences, The University of Arizona, 1630 E. University Blvd. #94, Tucson, AZ 85721, M. E. L. Jungwirth, E. L. Dereniak, and G. R. Gerhart are preparing a manuscript to be called, "White light Sagnac interferometer for snapshot multispectral imaging."
12. F. Snik, T. Karalidi, and C. Keller, "Spectral modulation for full linear polarimetry," *Appl. Opt.* **48** (7), 1337-1346 (2009).